Enhanced thermal stability of precipitates and elevated-temperature properties via microalloying with transition metals (Zr, V and Sc) in Al–Cu 224 cast alloys

Dong Li, Kun Liu*, Jovid Rakhmonov and X.-Grant Chen*

Department of Applied Science, University of Quebec at Chicoutimi, Saguenay, QC, G7H 2B1, Canada

* Corresponding authors: kun.liu@uqac.ca, xgrant_chen@uqac.ca

Abstract

The evolution of precipitates and the elevated-temperature mechanical and creep properties of Al–Cu 224 cast alloys with the microalloyed transition metals (TMs) of Zr, V, and Sc were investigated. The results showed that the addition of TMs can generally delay the transformation from θ″ to θ′ during T7 aging and can effectively increase the coarsening resistance of θ′ during prolonged thermal exposure (T7A), especially in the alloys with combined TM additions. Meanwhile, thermally stable $L1_2$-Al_3M dispersoids were observed in alloys with Zr and Sc+Zr additions. With the increased thermal stability of the predominant strengthener θ′, both the yield strength and creep resistance at 300 °C were remarkably improved. Under the T7A condition, the alloy with the combined Zr+V addition achieved the highest yield strength at 300 °C with an increase of 37% relative to the base alloy. The alloy microalloyed with Sc+Zr exhibited the best creep resistance with a minimum creep rate of 5.5×10^{-9} s^{-1} compared with 2.0×10^{-7} s^{-1} for the base alloy, owing to the co-existence of thermally stable θ′ and Al_3(Sc, Zr). The relationship between the evolution of the microstructure and the mechanical properties under the T7A condition was rationalized using the proposed strengthening mechanisms.

Keywords: Al–Cu cast alloys; Transition Metals; Precipitates; High-temperature strength; Creep resistance.

1. Introduction

In the past decades, cast aluminum alloys have been increasingly used in the automotive industry to reduce weight and improve fuel efficiency, such as the most popular cast Al–Si (e.g., 356 type) and Al–Si–Cu (e.g., 319 type) alloys because of their good castability and the high strength–to–weight ratio [1–3]. Their strength at room temperature is principally derived from precipitation hardening via nanoscale precipitates [4]. However, when those engine components are in service at elevated temperatures (>200–250 °C), the nanoscale precipitates formed during the aging treatment (under T6/T7 temper) undergo rapid coarsening, leading to a sharp drop in their mechanical properties [5, 6, 7]. Therefore, how to improve the elevated–temperature properties of aluminum alloys are becoming one of the key challenges for their industrial applications.

Al–Cu cast alloys (e.g., 206 and 224 types) are one of the most promising aluminum alloy systems for elevated–temperature applications (250–350 °C) benefiting from their excellent balance between room–temperature and elevated–temperature properties and their potential high–temperature stability [8–11]. It has been reported that Al–Cu 206 alloy possessed a YS of 390 MPa at room temperature under the T7 condition and a YS of still as high as 93 MPa at 300 ℃ after thermal exposure at 300 °C for 100 h following T7 [12], which is remarkably higher than those of reported Al–Si and Al–Si–Cu cast aluminum alloys. While the YS at 300 °C after thermal exposure at 300 °C reached 105 MPa with addition of Mn, Zr and Ni in Al–Cu 206 alloys [13], indicating the

enhancement on elevated-temperature properties with transition metals (TMs). Furthermore, recent work [8] reported the YS at 300 ℃ of Al–Cu 224 alloy could be further improved to 140 MPa after exposure at 300 °C for 100 h via microalloying with Mg, Zr, V, and Ti, demonstrating the significant contribution from transition metals (TMs). Besides the elevated-temperature YS, the creep resistance at 300 °C in Al–Cu based alloys is also reported to be enhanced by one of the TMs, such as Sc [14–17].

Two principal strengthening mechanisms have been proposed on the role of TMs in improving the elevated-temperature properties and thermal stability in Al–Cu alloys. It is well recognized that nanoscale θ′-Al_2Cu precipitates are the primary strengthening phase, but they are thermodynamically metastable. As the temperature increases (>250 °C), θ′-Al_2Cu rapidly coarsens and transforms to equilibrium θ-Al_2Cu, which loses its strengthening effect. One of the strengthening mechanisms via microalloying of TMs is the solute atoms of TMs segregated to the θ′ interfaces, contributing to the high-temperature stabilization of θ′ precipitates through diffusion barriers, solute drag, interfacial energy reduction, and lattice strain modifications [9-11, 13, 14, 16-18]. The interfacial solute segregation was well confirmed by the experimental results using scanning transmission electron microscopy (STEM) and atomic probe tomography (APT), although most studies have focused on Zr, Mn [10, 13] and Sc [14, 16, 17]. Another TM-strengthening mechanism involves the formation of thermally stable Ll_2-Al_3M dispersoids, promoting the nucleation of θ″/θ′ precipitates [14-16, 19-21], which improves elevated-temperature strength and particularly enhances the creep resistance at 300 °C. It has been confirmed that the formation of a large number of thermally stable dispersoids, such as α-dispersoids with Mn, Mo, and Cr, as well as Ll_2-Al_3M with Sc and Zr, could significantly improve the elevated-temperature mechanical and creep properties in 3xxx and 6xxx aluminum alloys [22–25]. Despite numerous investigations, systematic studies on the individual and combined effects of the addition of TMs on the elevated-

temperature properties in Al–Cu cast alloys are still limited in open literature. It is worthwhile to discover the contribution of TMs in Al–Cu alloys in stabilizing the precipitates, improving the elevated-temperature properties for further development, and optimizing the design of cast aluminum alloys in wide elevated-temperature applications.

The present work studied the effects of individual and selected combined additions of TMs (Zr, V, and Sc) on the thermal stability of precipitates and elevated-temperature properties of Al–Cu 224 alloy. Since Sc is generally always co-added with Zr, no individual Sc addition or combined Sc and V is designed in the present work. The evolution of both precipitates (θ″/θ′ and Ll_2-Al_3M) after T7 aging and during prolonged thermal exposure (T7A) were investigated and quantified by transmission electron microscopy and image analysis. The elevated-temperature properties, namely the YSs under T7 and T7A conditions and the creep properties at 300 °C, were experimentally determined. Attention was paid to the synergistic effect of the combined addition of TMs on the stabilization of the θ′ phase, the elevated-temperature YS, and the creep resistance. The strengthening contributions from the θ′ precipitates and the Ll_2-Al_3M dispersoids were evaluated under the proposed strengthening mechanisms.

2. Experimental procedure

Five Al–Cu 224 type cast alloys with different additions of Zr, V and Sc were prepared with Al–50%Si, Al–25%Mn, Al–5%Ti–1%B, Al–50%Cu, Al–5%V, Al–15%Zr, Al–15%Sc master alloys, pure Mg (99.9%) and commercial pure Al (99.8%). For each alloy, approximately 3.2 kg of prepared materials were melted in a clay graphite crucible using an electric resistance furnace. After maintaining at approximately 750 ℃ for 30 min with protective

atmosphere and degassing for 15 min with high purity Ar gas, the alloys were poured into a permanent steel mold preheated at 250 ℃ to cast the rectangular ingots with the dimension of 80mm×40mm×30mm. The chemical compositions were analyzed by an optical emission spectrometer and shown in Table 1.

Table 1. Chemical composition of experimental Al-Cu alloys (wt.%)

Alloys	Si	Fe	Cu	Mg	Mn	Ti	Zr	V	Sc	Al
B	0.12	0.13	4.9	0.13	0.38	0.11	–	–	–	Bal.
Z2	0.10	0.13	4.9	0.11	0.36	0.10	**0.18**	–	–	Bal.
V2	0.10	0.13	4.8	0.13	0.38	0.10	–	**0.25**	–	Bal.
ZV	0.08	0.13	4.7	0.12	0.35	0.09	**0.15**	**0.13**	–	Bal.
SZ	0.09	0.12	4.4	0.11	0.33	0.08	**0.15**	–	**0.16**	Bal.

After casting, the experimental alloys were solution-treated with a 2-step method (495℃/2h + 523℃/10h) followed by water quenching. Generally, overaging (T7) is performed for Al-Cu alloy in industries to achieve the balance between strength and corrosion resistance. Therefore, T7 aging treatment at 200 ℃ for 4 hours was also performed in the present work, referred to as T7 samples. Some of the T7-treated ones were further held at 300 ℃ for 100 hours. These samples after thermal exposure were referred to as T7A samples, as illustrated in Fig. 1.

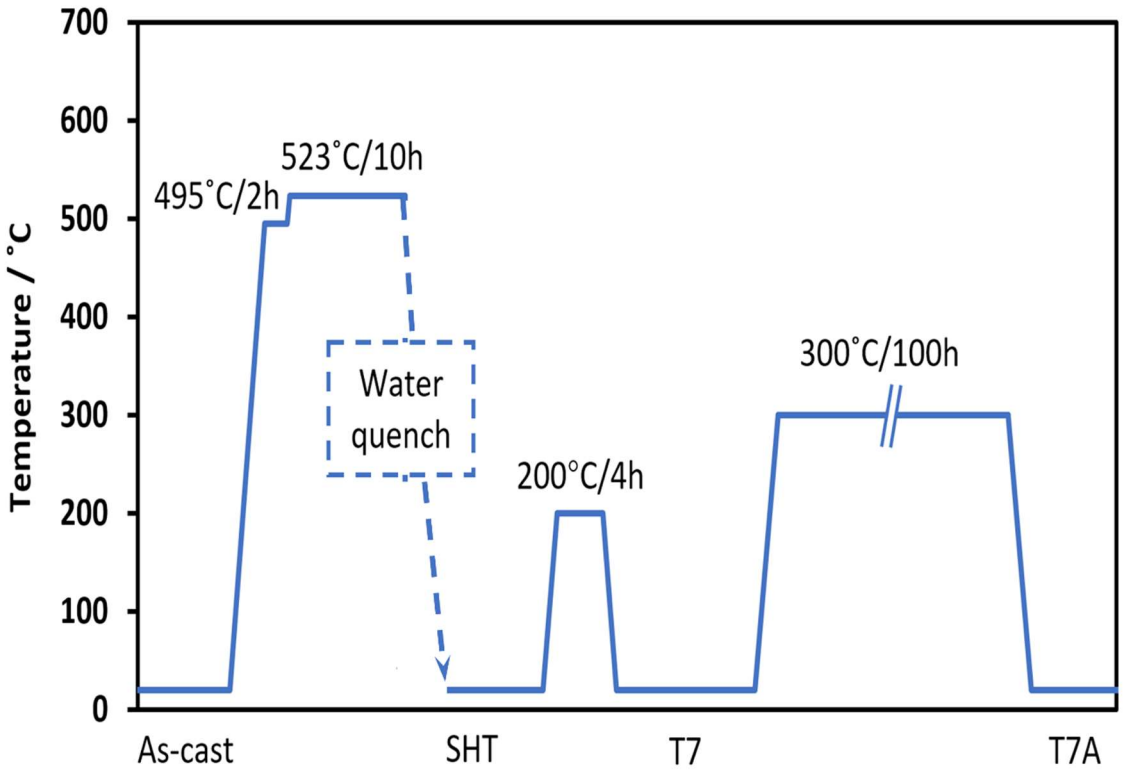

Fig. 1. Heat treatment procedures of experimental alloys

Vickers microhardness was measured using an NG-1000 CCD micro-hardness test machine with a 25g load and 15s dwelling time. 10 measurements were performed on the aluminum matrix to obtain the average value for each polished sample. The compressive yield strength (YS) at room temperature and 300 ℃ was measured using a Gleeble 3800 system with a total strain of ~0.4 and a fixed strain rate of $0.001s^{-1}$. The creep tests were performed at 300 °C for 100 hours in the compression condition with a constant load of 50 MPa on T7A samples. The specimens for both YS and creep tests were machined to cylinders with 10 mm in diameter and 15 mm in height. Each condition was repeated at least 3 times to get the average value.

The evolution of intermetallics in as-cast and heat-treated conditions was characterized by a scanning electron microscope

(SEM, JSM-6480LV) equipped with an energy dispersive X-ray spectrometer (EDS). To investigate the θ˝/θ′ precipitates and Al_3M dispersoids in detail, a transmission electron microscope (TEM, JEOL JEM-2100) operated at 200kV with STEM-EDS were employed. The TEM foils were punched to 3 mm in diameter and then polished to approximately 50 μm in thickness, followed by twin-jet electrochemical polishing at 15 V DC in a 30 % nitric acid and 70 % methanol solution at −20 °C. The Convergent Electron Beam Diffraction (CBED) technique was used to estimate the thickness of TEM specimens in present work. The obtained TEM images were analyzed by ImageJ analysis software to quantify the precipitates and dispersoids. Since the morphology of θ˝/θ′ precipitates and Al_3M dispersoids are different, and therefore they were characterized with following different equations.

The perfect disk shape is assumed for simplification for θ″/θ′-Al_2Cu precipitates. Due to the truncation of θ″/θ′ precipitates at the foil surfaces, a modification (Eq. 1) was made to get the true diameter d_p based on the measured mean length l_p from the image analysis on TEM images taken with the thickness of foil t [26]:

$$d_p = \frac{2(l_p - t) + 2\sqrt{(l_p - t)^2 + \pi l_p t}}{\pi} \quad (1)$$

The number density N_v was calculated based on the measured number of precipitates (N_p) along the 2 explicit $(001)_{Al}$ directions in TEM images with the area of A_s, using the following equation [27, 28]:

$$N_v = N_p \frac{\left(1 + \frac{t + d_p}{2\sqrt{A_s}}\right)}{A_s(t + d_p)} \quad (2)$$

For the near-spherical Al_3M dispersoids, their number density N_v was calculated as:

$$N_v = \frac{N_d}{A_s(t+d_d)} \quad (3)$$

where, N_d is the number of Al_3M counted in the TEM images, t is the thickness of observing area in TEM and d_d is the calculated average diameter of Al_3M dispersoids.

3. Results

3.1 As-cast and as-solutionized microstructures

In the present work, it was found that alloys B, Z2, V2, and ZV have similar types of intermetallics in the as-cast state, which consist of dominant θ−Al_2Cu, mixed Fe−rich intermetallics (Fe−IMCs) of β−Al_7Cu_2(Fe, Mn) and α−Al(Fe, Mn)Si [29], as shown in the example of the alloy ZV (Fig. 2a). The addition of Zr and V did not lead to the noticeable formation of primary V- and Zr-containing intermetallics [30], indicating that most of the Zr and V alloying elements were well saturated in the aluminum matrix after casting. This was confirmed by the as-cast microhardness (Fig. 3), which is increased from alloy B to Z2, then V2, and further to ZV owing to the solid solution hardening of TMs. After the solution treatment (Fig. 2b), most of the θ−Al_2Cu phases dissolved into the matrix, leading to a significant increase in the microhardness in the as−solutionized state (Fig. 3). However, Fe−IMCs remained in the matrix because of their high melting points [31].

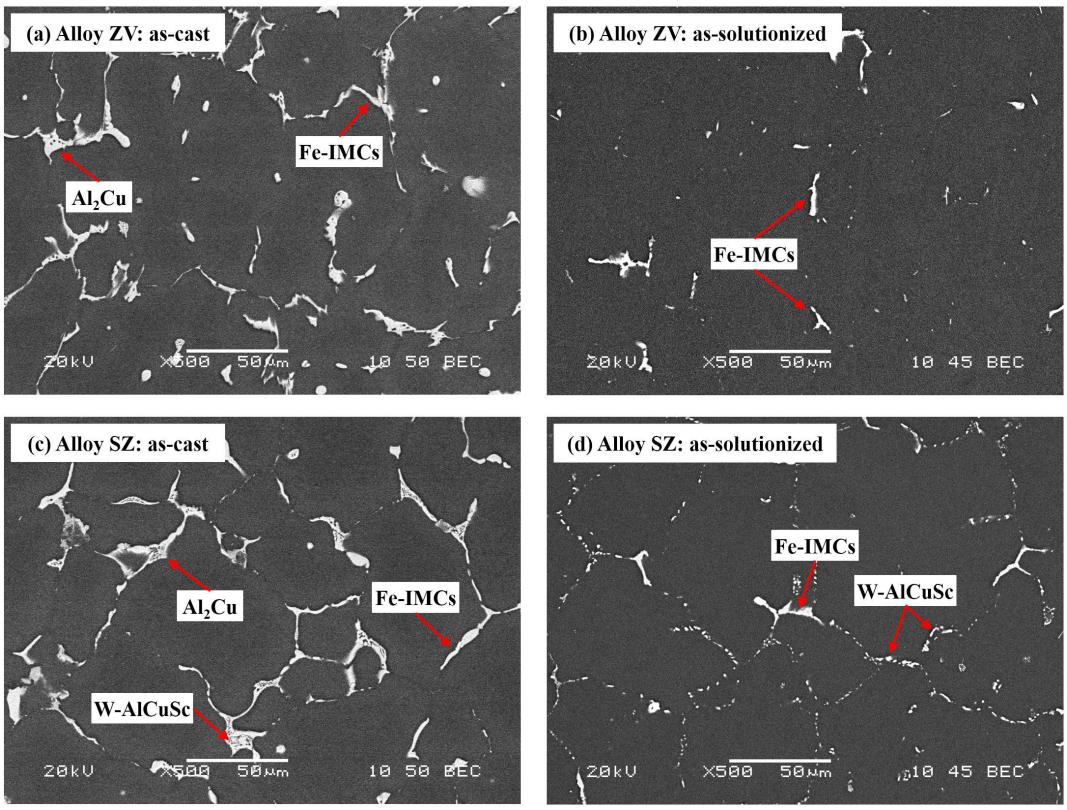

Fig. 2. Intermetallic type and distribution in the alloy ZV (a, b) and the alloy SZ (c, d) under as-cast (a, c) and as-solutionized (b, d) conditions.

However, in the alloy SZ, as shown in Fig. 2(c), an additional intermetallic phase was observed in addition to those intermetallics found in the other alloys (Fig. 2a), which was identified as the W–AlCuSc phase using SEM–EDS results and information from [32]. Although the W phase was partially fragmented during the solution treatment, it was still distributed along the dendrite boundaries (Fig. 2d). Because of the formation of the W phase during both solidification and solution treatment [32], it consumed the Cu and Sc solutes in the matrix and hence reduced their solid solution strengthening,

resulting in a lower microhardness relative to the alloys ZV, Z2, and V2 in both as-cast and as-solutionized conditions (Fig. 3).

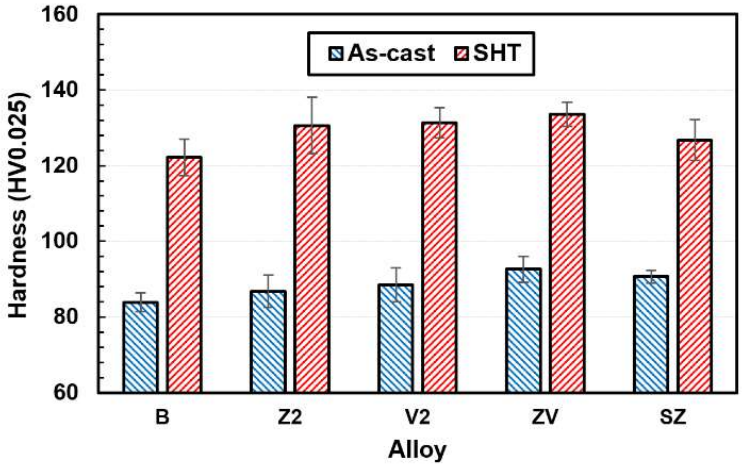

Fig. 3. Vickers microhardness of the experimental alloys under as-cast and as-solutionized (SHT) conditions.

3.2 Evolution of precipitates under T7 and T7A conditions

3.2.1 Precipitation under T7 condition

Fig. 4 shows the typical bright-field (BF) TEM images and the corresponding selected area diffraction patterns (SADPs) of the experimental alloys under the T7 condition. The microstructures of all alloys revealed that the predominant precipitates along the $<001>_{Al}$ directions were the cross-sections of the disk-shaped θ″- and θ′-Al_2Cu precipitates that typically appear in the grain interiors of the (near-) peak-aged Al-Cu alloys [8, 12, 33]. Predominant θ′ precipitates were present in the base alloy (alloy B in Fig. 4a), while a mixture of both θ″ and θ′ precipitates was observed in the alloys with TMs (Fig. 4b-4e). This is consistent with the SADPs (insets in the corresponding images in Fig. 4), in which the characteristic features of θ′ can be seen in all alloys, but those of θ″ are solely observed in the alloys modified with TMs. These observations

imply that the microalloying of TMs, particularly when added in combination, could slow the transformation of θ″ into the θ′ phase during aging. Owing to the low diffusivity of TMs in the α-Al matrix, as well as their high vacancy binding energies, the diffusion of Cu atoms in the matrix becomes sluggish during aging, resulting in slower aging kinetics relative to the base alloy [20].

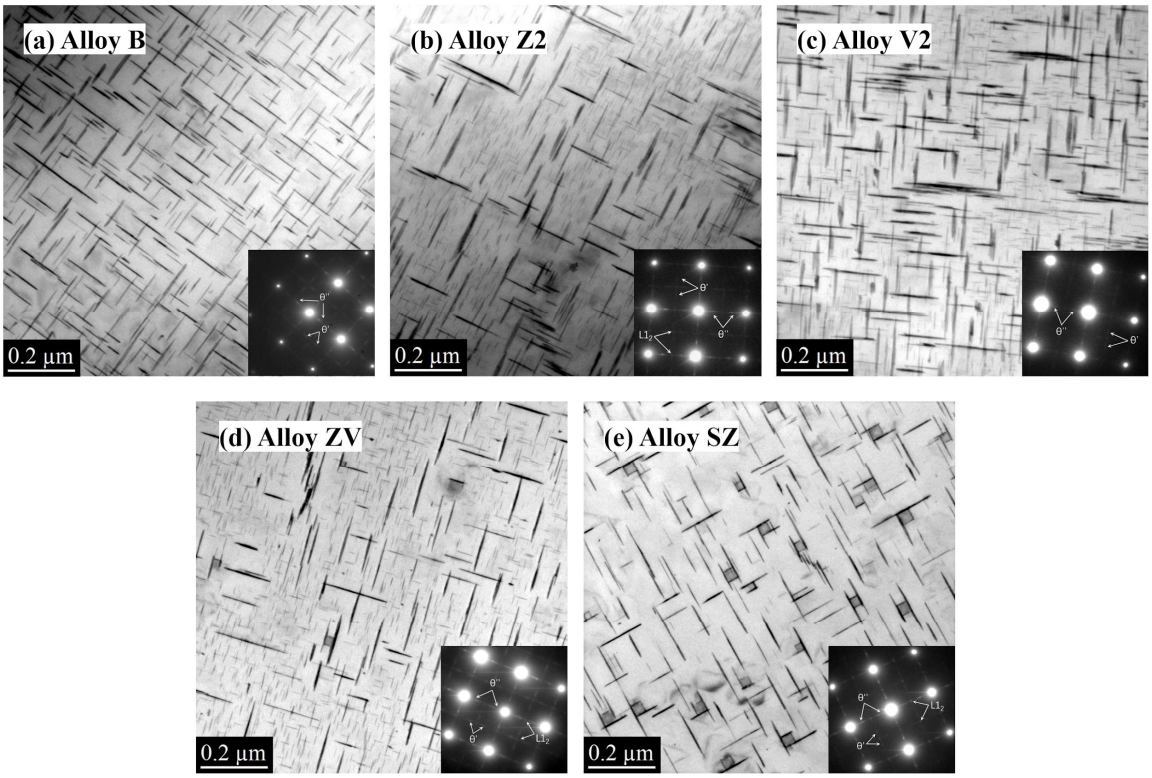

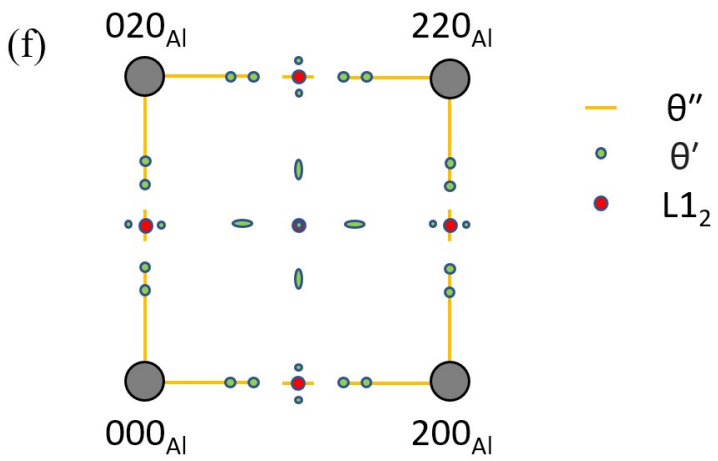

Fig. 4. (a-e) Bright-field TEM images of experimental alloys under T7 condition showing θ″/ θ′ precipitates with the corresponding SADPs. (f) Schematic diagram of the diffraction patterns based on experience.

The θ′ precipitates exhibited similar dimensions in all experimental alloys, within measurement error, with the average diameter, d_p, ranging between 98 and 123 nm and the average thickness, t_p, varying between 6.3 and 6.8 nm (Table 2). The θ″ precipitates appeared much finer than the θ′ precipitates, with an average diameter of 28−34 nm and an average thickness of ~3 nm (Table 2). Another distinctive feature between the Sc-added alloy (SZ) and other alloys modified with Zr and V was a relatively lower number density of both θ″ and θ′ precipitates (Table 2). This is most likely attributed to the presence of an insoluble W phase formed during solidification and solution treatment (Fig. 2c and d), which reduced the supersaturated level of Cu solutes in the matrix during T7 treatment.

Table 2. Quantitative parameters of θ″, θ′ and $L1_2$-Al_3M precipitates under T7 condition

Alloy code	Type of precipitates	d_p (nm)	t_p (nm)	d_d (nm)	N_v (μm^{-3})
B	θ″	34.4±11.5	2.9±0.4		540
	θ′	101.6±34.4	6.6±1.2		972
Z2	θ″	28.6±9.3	2.9±0.4		8075
	θ′	105.1±36.0	6.5±1.6		667

	$L1_2 - Al_3(Zr)$			20.4±4.9	335
V2	θ″	29.6±7.8	3.0±0.4		3514
	θ′	109.9±31.2	6.3±1.0		767
ZV	θ″	28.1±7.0	2.9±0.2		10848
	θ′	98.2±29.3	6.2±1.3		697
SZ	θ″	35.3±8.7	3.9±0.4		917
	θ′	122.7±47.3	6.8±1.1		447
	$L1_2 - Al_3(Sc,Zr)$			30.7±6.3	192

In addition to the predominant θ″/θ′ precipitates, the $L1_2$-Al_3M dispersoids were observed mainly in alloys Z2 and SZ, which were revealed by the dark field images of the {100} superlattice reflections of precipitates along the <110> or <100> zone axis (Fig. 5) and substantiated by the reflection spots at the $\{100\}_{Al}$ and $\{110\}_{Al}$ positions in the corresponding SADPs (Fig. 4). Those spherical dispersoids formed during solution treatment exhibited a relatively large size (d_d of ~20 nm in Z2 and d_d of ~30 nm in SZ, as listed in Table 2). The dispersoids were identified as $Al_3(Zr)$ and $Al_3(Sc,Zr)$ in the alloys Z2 and SZ, and the number densities of the dispersoids were measured as 335 and 192 μm^{-3}, respectively (Table 2). It is evident that the base alloy has no dispersoid, and the V addition (alloy V2) seems to have no dispersoid-forming ability under the given composition, as no V-rich dispersoids could be observed, which is probably attributed to the relatively high solid solubility of V in the α−Al matrix [34]. The presence of V also disfavored the precipitation of $L1_2$-Al_3M dispersoids, as a much lower quantity of Al_3M dispersoids were observed in the combined addition of Zr and V (alloy ZV, Fig. 5b) compared to the individual addition of Zr (alloy Z2, Fig. 5a).

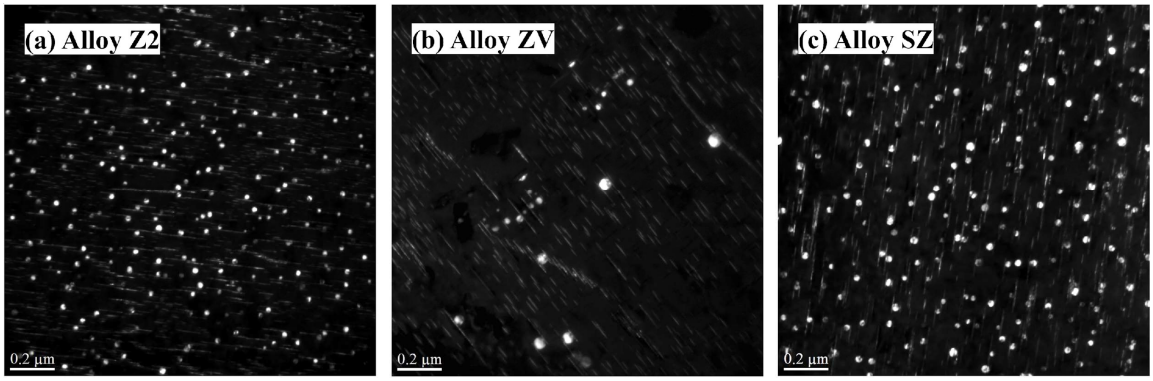

Fig. 5. Dark-field TEM images for alloys of Z2 (a), ZV (b) and SZ (c) under T7

3.2.2 Evolution of precipitates and their thermal stability at elevated temperature

The thermal stability of the precipitates was assessed by exposing the T7-treated samples at 300 °C for 100 h (T7A). One obvious feature is that θ″ was completely transformed into θ′, and θ′ gradually coarsened during thermal exposure at 300 °C in all experimental alloys (Fig. 6). However, no evidence of the presence of equilibrium θ was observed yet in all alloys. Moreover, the characteristics of θ′ after T7A varied significantly from one alloy to another (Fig. 6 and Table 3), indicating the important role of TMs in the coarsening kinetics of θ′ precipitates and their thermal stability, as reported in several studies related to the addition of TMs to the Al−Cu system [8, 10, 13, 14, 16]. In addition, the $L1_2$-Al_3M dispersoids, unlike the θ′ precipitates, showed no coarsening tendency during thermal exposure at 300 °C for up to 100 h, as their size remained almost unchanged relative to the T7-treated samples (Table 3 vs. Table 2), owing to their excellent thermal stability and low diffusion rates of Zr and Sc in the α−Al matrix at 300 °C [35].

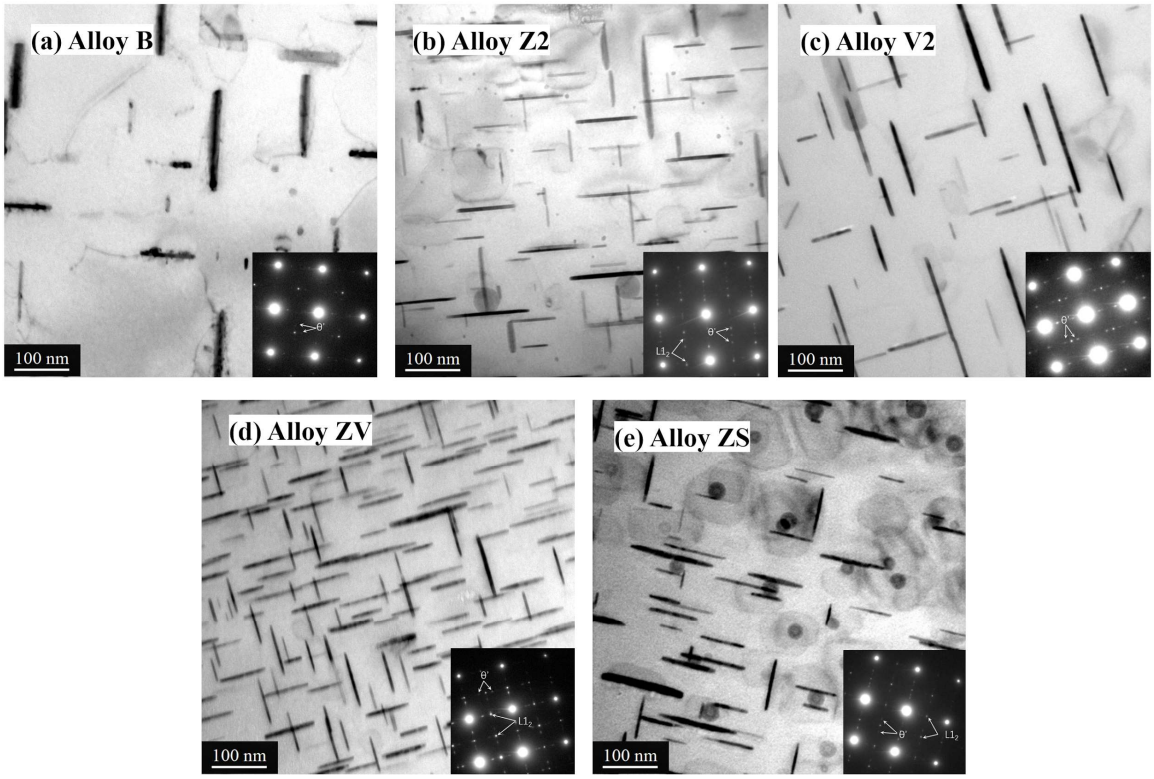

Fig. 6. Bright-field TEM images of experimental alloys under T7A.

Table 3. Quantitative TEM results of θ′ precipitates and $L1_2$-Al_3M dispersoids in the thermally exposed T7A samples

Alloy code	Type of precipitates	d_p (nm)	t_p (nm)	d_d (nm)	N_v (μm^{-3})
B	θ′	139.5±96.9	13.0±5.9		139
Z2	θ′	87.9±44.6	8.1±2.3		403
	$L1_2-Al_3$(Zr)			20.6±5.8	315
V2	θ′	122.5±59.6	9.3±2.4		228
ZV	θ′	81.6±31.2	6.8±1.0		649
SZ	θ′	82.6±33.7	8.9±1.6		397
	$L1_2$ − Al_3(Sc,Zr)			29.6±8.0	211

The θ′ precipitates in the base alloy B after T7A were severely coarsened (Fig. 6a), possessing the average thickness, t_p, of 13.0 nm and the average diameter, d_p, of 139.5 nm. Coarsening of θ′ resulted in a significant decrease in its number density, N_v, from 972 μm^{-3} under T7 (Table 2) to 139 μm^{-3} after T7A (Table 3). In contrast, alloy Z2 with individual Zr addition after T7A exhibited a microstructure composed of much finer θ′ precipitates (Fig. 6b) with a t_p of 8.1 nm and a d_p of 87.9 nm (Table 3). Consequently, the N_v of the θ′ precipitates in alloy Z2 was much higher than that in alloy B (403 vs. 139 μm^{-3}). The results demonstrate the role of Zr in enhancing the thermal stability of θ′ precipitates, confirming the findings of recent studies [10, 13]. Several studies have reported that Zr can segregate to the coherent and semi-coherent interfaces between Al and θ′-Al_2Cu to reduce its interfacial energy [10, 11, 18], thus providing a lower driving force for precipitate coarsening. Zr solute atoms enriched at the θ′ interfaces could also act as a diffusion barrier, thus kinetically slowing the coarsening of the θ′ phase [18].

The θ′ precipitates in alloy V2 with individual Zr addition after T7A were considerably finer than those in alloy B (Fig. 6c and Table 3), but they are relatively coarser with a lower N_v than those in alloy Z2. This suggests that V also exhibited a stabilizing effect on θ′, but its efficiency was inferior to that of Zr. Although no study has reported so far the beneficial effect of V on stabilizing the θ′ phase, the mechanism for stabilizing θ′ in the present study is believed to resemble the effect of Zr addition owing to the close chemical homology between Zr and V [36].

Among the alloys studied, the finest θ′ precipitates with the highest N_v were obtained in alloy ZV after T7A (Fig. 6d and Table 3). Clearly, with the combined presence of Zr and V, the coarsening of θ′, particularly the thickening, became significantly reduced, which allowed for a very high N_v of θ′ precipitates (649 μm^{-3}) in the microstructure. The t_p of θ′ in alloy ZV (6.8 nm) is the lowest among all alloys and almost twice thinner than that of θ′ precipitates in alloy B (Table 3). These results suggest that co-presence of Zr and V at the θ′ interfaces significantly reduce their coarsening (thickening) by disfavoring the ledge nucleation and growth which control the thickening of the θ′ phase [37].

The N_v of θ′ in alloy SZ after T7A was remarkably lower than that in alloy ZV (397 vs. 649 μm^{-3}) (Table 3). Moreover, although a higher number density of finer θ′ precipitates

can be observed in the alloy SZ than in alloys B and V2 (Fig. 6e and Table 3), the average thickness of θ′ precipitates (t_p), which is the most important parameter in describing the interface-controlled coarsening of platelets, was remarkably larger in alloy SZ than in alloy ZV. It was confirmed by some studies [14, 16] that Sc could also segregate to the θ′-Al_2Cu interfaces to reduce its interfacial energy and act as a diffusion barrier for Cu atoms, thus slowing the coarsening of the θ′ phase at elevated temperatures. However, the obtained results suggest that the co-presence of Sc and Zr is not as effective as the co-presence of Zr and V in reducing the thickness growth of θ′.

3.3 Evolution of elevated-temperature strength and creep properties

3.3.1 Yield strength under T7 and T7A conditions

As shown in Section 3.2, the evolution of precipitates and their thermal stability vary greatly with the microalloying of TMs. Therefore, it is expected that these changes will yield various properties, especially at elevated temperatures after thermal exposure (T7A). In the present work, the compressive YSs at both room temperature (RT) and 300 °C under T7 and T7A conditions were measured, and the results are summarized in Fig. 7. As shown in Fig. 7a, the YS at RT under the T7 condition moderately increased with the addition of Zr and V compared with the base alloy, but then decreased with the combined additions of Sc and Zr (alloy SZ). For instance, the YS at RT gradually increased from 321 MPa in base alloy B to 331–332 MPa in alloys Z2 and V2, and further increased to 337 MPa in alloy ZV, but sharply dropped to 272 MPa in alloy SZ. When the test temperature was increased to 300 °C, the YS values at 300 °C under the T7 condition were significantly reduced owing to the reduced shear modulus of the α−Al matrix at elevated temperatures. However, the variation tendency was the same as that of the YS at RT. For instance, the YS at 300 °C increased from 153 MPa in base alloy B to 165 MPa in alloy ZV, but then decreased to 147 MPa in alloy SZ. In general, the microalloying addition of Zr and V can moderately improve the YS after T7 aging, which is attributed to a modest increase in the amount of θ″/θ′ precipitates and the formation of $L1_2$-Al_3M dispersoids in the experimental alloys [10, 12]. However, the lower YS of the alloy SZ compared to that of the base alloy is less

expected, which is principally contributed to the considerably lower amount of θ″/θ′ due to less available Cu solutes caused by the formation of the W phase.

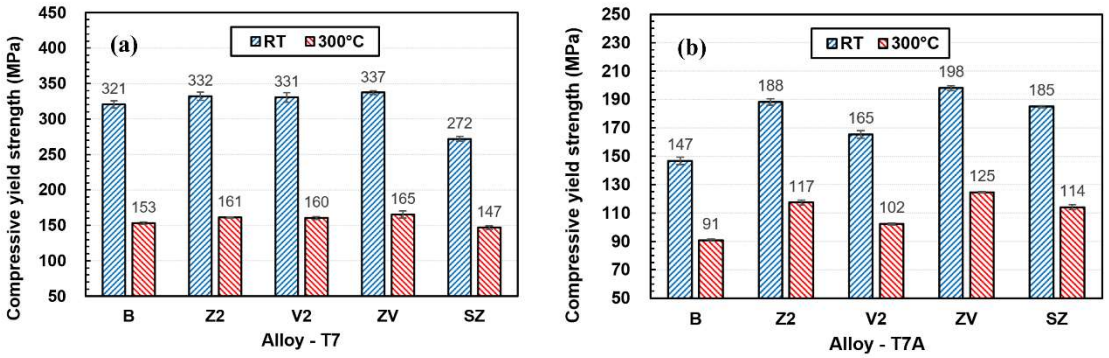

Fig. 7. Compressive YS at both RT and 300 ℃ under T7 (a) and T7A (b) conditions.

Fig. 7(b) illustrates the evolution of the YS of the experimental alloys after thermal exposure at 300 °C for 100 h, in which the YSs under the T7A condition were much lower than those under the T7 condition, which can be contributed to the coarsening of θ″/θ′ precipitates, as shown in Fig.6 and Table 3 for T7A compared with that in Fig. 5 and Table 2 for T7. Compared with Fig. 7(a), the YSs at RT and 300 °C of alloy B decreased from 321 MPa and 153 MPa, respectively, after T7 aging to 147 MPa and 91 MPa, respectively, under the T7A condition. This high percentage decrease in YS (54% at RT and 41% at 300 °C) is closely related to the coarsening resistance of the θ′ precipitates. As shown in Fig. 6a, during thermal exposure, the thermal stability of θ′ in base alloy B is very poor, resulting in much coarser θ′ precipitates with a lower number density under the T7A condition compared to the T7 samples. However, the percentage decrease is remarkably lower in alloys with added TMs, especially in alloys ZV and SZ, indicating the improved thermal stability of θ′ with microalloying of Zr, V, and Sc. As shown in Fig. 7(b), the YSs of the alloy ZV under T7A at RT and 300 °C were 198 MPa and 125 MPa, respectively, and the decrease percentages were 41.2% and 24.2%, respectively. The alloy SZ also presents higher YSs under T7A (186 MPa at RT and 114 MPa at 300 °C) and lower decrease percentages (32.0% at RT and 22.4% at 300 °C) relative to the base alloy B. As demonstrated in Fig. 6, the alloys ZV and SZ exhibited excellent coarsening resistance of θ′ precipitates during thermal exposure at 300 °C. As an important mechanical property for

high-temperature applications, the YS at elevated temperature (300 °C) increased steadily from 91 MPa (alloy B) to 102 MPa (alloy V2), 114 MPa (alloy SZ), 117 MPa (alloy Z2), and 125 MPa (alloy ZV), which represented an improvement of 12.1% for alloy V2, 25.3% for alloy SZ, 28.6% for alloy Z2, and 37.4% for alloy ZV, respectively. This confirms the important role of TMs in improving the microstructural stability and hence elevated-temperature strength of Al−Cu alloys.

3.3.2 Creep resistance under T7A condition

Creep resistance, one of the most important elevated-temperature properties [23], was measured with a constant load of 50 MPa at 300 °C for 100 h for the samples after thermal exposure (T7A). The typical creep curves as a function of the creep time are shown in Fig. 8. From the results of Fig. 8a, it can be observed that the creep strain of the base alloy B increased constantly with time, and the total creep strain after 100 h reached a very high level (0.23), which was significantly higher than that of the other four alloys with the addition of TMs. As shown in the enlarged creep curves in Fig. 8b, the total creep strains were only 0.04, 0.015, 0.008, and 0.007 for alloys V2, Z2, ZV, and SZ, respectively.

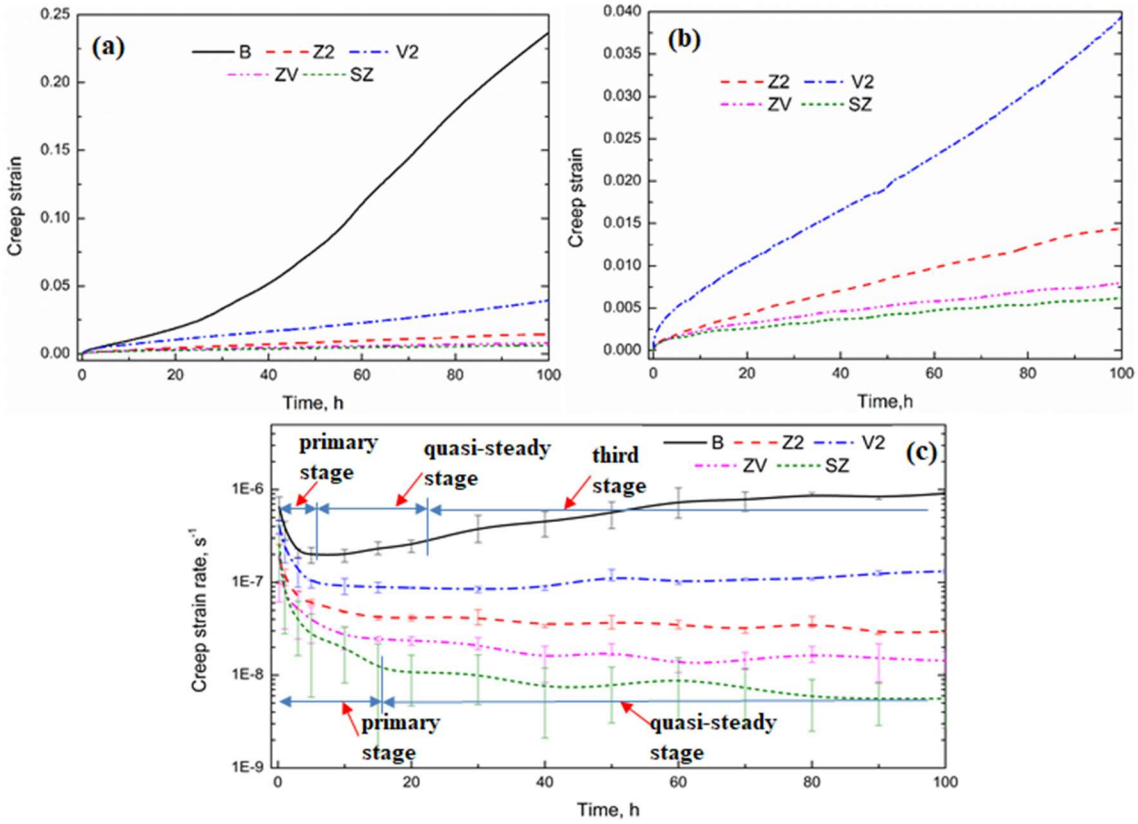

Fig. 8. (a) Typical creep curves, (b) enlarged view of creep curves, and (c) the creep strain rate curves of experimental alloys under T7A condition.

The evolution of the creep strain rate with the creep time is shown in Fig. 8c. During compressive creep deformation, the creep rate initially decreases rapidly, which can be defined as the primary stage. With increasing time, the creep rate tends to be stable and reaches a quasi-steady stage. The average creep rate at the quasi-steady stage is calculated as the minimum creep rate [38]. After this stage, the creep enters the third stage, often encountered in relatively soft materials, at which the creep rate continuously increases [39]. As shown in Fig. 8c, alloy B possessed short primary and quasi-steady stages, and creep ended at the third stage just after ~20 h, indicating a poor creep resistance. However, the other four alloys with the addition of TMs remained at the quasi-steady stage after the relatively short period of the primary stage. Meanwhile, the minimum creep rates of alloys with added TMs were much lower than that of alloy B. As shown in Fig. 8c, the minimum creep rates of alloys V2, Z2, ZV and SZ are calculated as 8.4×10^{-8}, 2.8×10^{-8}, 1.3×10^{-8},

and 5.5×10^{-9} s^{-1}, respectively, compared with 2.0×10^{-7} s^{-1} for alloy B. Therefore, the lower value of both creep strain and the minimum creep rate of alloys with added TMs confirm the remarkable contribution of TMs to the enhancement of creep resistance. Based on the data of the creep strain and minimum creep rate, the creep resistance at 300 °C is increasing from alloy B to V2, Z2, ZV and further to SZ.

As a summary from 3.2 and 3.3, the additions of TMs generally improve the mechanical properties, especially the YS and creep resistance at 300 °C, which is in consistent with the literature [13–17]. In previous work, with addition of Mn, Zr and Ni, the YS at 300 °C in Al–Cu 206 type alloys is improved from 93 to 105 MPa [12, 13] while it was further improved to 140 MPa with Ti, Zr, and V additions in 224 alloys [14], which is similar to the case of present work from alloy B (91 MPa) to Z2 (117 MPa) and ZV (125 MPa). Meanwhile, the creep resistance was reported to enhanced ~ 10 times with the addition of Sc [14–16], which also confirms our finding in the present work. For instance, with additions of Zr (alloy Z2), the minimum creep rate is decreased to 2.8×10−9 s−1 from 2.0×10−7 s−1 of base alloy, which is ~10 times lower.

4. Discussion

4.1 The relationship between microstructure and yield strength

In heat-treatable Al–Cu alloys, the main precipitation sequence of the strengthening phases can be described as follows [40, 41]:

Supersaturated solid solution → atomic clusters → GP(I) zones → θ″ → θ′ → θ

It is well known that the YS at room temperature of Al–Cu alloys after aging is principally controlled by nanoscale θ″/θ′ precipitates. The results in Fig. 2 and Table 2 show that the addition of TMs delays the transformation from θ″ to θ′ and significantly increases the amount of θ″ under the T7 condition. However, it seems that the strengthening contributions from θ″/θ′ precipitates of all alloys, except alloy SZ, are similar because the

YSs at room temperature of the alloys are in the same narrow range (320–340 MPa, Fig. 7a). The slight increases in YSs through the addition of Zr and V in alloys Z2, V2, and ZV are associated with additional solid solution strengthening (alloys V2 and ZV) and $Al_3(Zr)$ dispersoid strengthening (alloy Z2). It is noticed that both additional strengthening effects play an insignificant role because of the predominant and efficient strengthening of θ″/θ′ precipitates under the T7 condition. The alloy SZ displays the lowest YS among all alloys (Fig. 8a), and even the precipitation of a reasonable amount of $Al_3(Sc, Zr)$ dispersoids cannot compensate for this, mainly because of the lower amount of θ′ and θ" precipitates compared to other alloys (Table 2). In general, the YS at 300 ℃ of the aluminum alloy is much lower than that at RT because of the softening of the aluminum matrix at elevated temperatures. However, the trend of YS changes induced by microalloying of TMs is the same as the trend at RT (Fig. 7a), because the YS at 300 °C under the T7 condition is still principally controlled by θ″/θ′ precipitates, as they are not yet coarsened.

During the prolonged thermal exposure at 300 °C for 100 h (T7A), all θ″ transformed to θ′, and θ′ coarsened. Therefore, the YS at the T7A state is mainly controlled by the precipitate parameters (number density and size) of θ′ resulting from the coarsening resistance of θ′ during thermal exposure. The higher the N_v of θ′ with finer size, the higher the coarsening resistance of θ′, and consequently, the higher the YS. Meanwhile, the presence of thermally stable Al_3M dispersoids would play a larger role in the alloy strength under the T7A condition relative to the T7 condition. As mentioned above, the addition of TMs (individual and combined) greatly increased the N_v of θ′ and refined the size of θ′ (Fig. 6 and Table 3), and hence remarkably increased the YS in the T7A state (Fig. 7b). The observed difference in the mechanical strength of the experimental alloys arising from θ′ precipitates and Al_3M dispersoids can be better explained by constitutive equations adopting strengthening mechanisms.

The contribution of the θ′ precipitates, which are non-shearable, to the critically resolved shear stress (CRSS) due to Orowan bypassing of θ′ is described by a modified Orowan equation [27]:

$$\Delta\tau_{\theta'} = \frac{Gb}{2\pi\sqrt{1-v}}\left(\frac{1}{1.23\frac{1.030}{\sqrt{N_v d_p}} - \frac{\pi d_p}{8} - 1.061 t_p}\right) ln\ ln\ \frac{0.981\sqrt{d_p t_p}}{b} \quad (4)$$

For spherical Al_3M dispersoids with d_d of 20−30 nm (Table 3), which are also non−shearable, an increase in CRSS occurs owing to the Orowan bypass mechanism, which is expressed by [20]:

$$\Delta\tau_{L1_2} = \frac{Gb}{2\pi\sqrt{1-v}}\left(\frac{1}{\frac{1.075}{\sqrt{N_v d_d}} - \frac{\pi d_d}{4}}\right) ln\ ln\ \frac{\pi d_d}{4b} \quad (5)$$

where G is the shear modulus of the α−Al matrix, v is the Poisson ratio (0.33 for Al), and b is the magnitude of the Burgers vector for aluminum (0.286 nm) [42]. For the calculation of the CRSS increment at room temperature arising from both θ′ precipitates and Al_3M dispersoids, G is taken as 28.0 GPa at 20 °C [20]. To predict the CRSS increment at 300 °C, Eqs. 4 and 5 are used for the first approximation. The only change is the shear modulus of the α−Al matrix, G, which is reduced from 28.0 GPa at 20 °C to 21.2 GPa at 300 °C [43].

The overall increments in CRSS due to θ′ and Al_3M phases are given by the following ad hoc superposition law with exponents suggested by literature [44]:

$$\Delta\tau_{ppt} = (\Delta\tau_{\theta'}^2 + \Delta\tau_{L1_2}^2)^{0.5} \quad (6)$$

The yield strength increases due to the precipitates and dispersoids present in grains interiors is obtained by [20]:

$$\Delta\sigma_{ppt} = M \cdot \Delta\tau_{ppt} \quad (7)$$

where, M(= 3.06) is the Taylor factor for polycrystalline fcc alloys [27]. The calculated values in the T7A state using the observed precipitate and dispersoid parameters (Table 3) are listed in Table 4.

For simplicity, it is assumed that the strengthening effects of other factors, such as solid solution hardening and grain size hardening, are relatively insignificant, and they are similar in all experimental alloys after T7A. Therefore, the YS values at RT and 300 °C for

the 1100-O alloy, 35 and 14 MPa [41], respectively, were added to the $\Delta\sigma_{ppt}$ values in a linear manner to the estimated YS of each alloy, and the results are listed in Table 4.

Table 4. Strengthening contributions of θ′ and $L1_2-Al_3M$ and comparison of between calculated and experimentally measured YSs at 20 ℃ and 300 ℃ in T7A state.

Alloys	Quantified precipitates	$\Delta\tau$ at 20 ºC (MPa)	$\Delta\tau$ at 300 ºC (MPa)	Calculated / measured YS at 20 ºC (MPa)	Calculated / measured YS at 300 ºC (MPa)
B	θ′	35.2	26.6	143 / 147	96 / 91
Z2	θ′	41.2	31.2	183 / 188	126 / 117
	$L1_2-Al_3Zr$	15.4	11.7		
V2	θ′	40.5	30.7	159 / 165	108 / 102
ZV	θ′	50.5	38.2	190 / 198	131 / 125
SZ	θ′	39.1	29.6	180 / 185	124 / 114
	$L1_2-Al_3$(Sc,Zr)	16.8	12.7		

The calculated YSs at both RT and 300 °C show good agreement with those experimentally measurements for all alloys studied, indicating that the Orowan dislocation bypass strengthening mechanisms of both θ′ precipitates and Al_3M dispersoids may control the alloy strength in the T7A state. Undoubtedly, θ′ appears to be the major alloy strengthener in all the alloys studied. The increment in CRSS at both 20 °C and 300 °C due to θ′ in base alloy B is much lower than that in the TM-added alloys owing to alloy B having the weakest coarsening resistance of θ′ during thermal exposure. The order of the CRSS increment due to θ′ can be listed as follows: alloy ZV (~50 MPa at 20 °C) > alloys Z2, V2, and SZ (~40 MPa at 20 °C) > alloy B (~35 MPa at 20 °C). The trends at both 20 °C and 300 °C were the same. These results imply that the combined addition of Zr and V (alloy ZV) is more effective than the individual addition of Zr or V (alloys Z2 and V2). The high number density of fine θ′ precipitates of alloy ZV after T7A indicated that alloy ZV had the highest coarsening resistance of θ′, and it rendered this alloy the highest YS of 198 MPa at 20 °C and 125 MPa at 300 °C, respectively (Fig. 7).

The results in Table 4 also show that the presence of thermally stable Al_3M dispersoids formed during solution treatment, contributed considerably to the overall increments in CRSS under T7A conditions, although the number density of Al_3M was quite limited in the current solution treatment condition. For instance, the contribution of Al_3Zr in alloy Z2 was 27% of the overall CRSS increments, while the contribution of Al_3(Sc, Zr) in the alloy SZ reached 30%, which provides a complementary strengthening effect on high-temperature YS. Although the additional strengthening of Al_3M dispersoids in the alloys Z2 and SZ is still minor, tailoring solutionizing parameters to obtain a higher N_v of finer Al_3M dispersoids could further improve the high-temperature strength [14, 20].

4.2 Relationship between microstructure and creep resistance

According to the creep mechanism map [45] and the literature [16], the creep deformation of experimental alloys is likely controlled by the dislocation creep mechanism under the current creep condition (50 MPa at 300 °C). Therefore, the factors influencing the dislocation movement during creep deformation would determine the creep resistance of the material, which were the major microstructural constituents that remained after T7A, e.g., θ′ precipitates and $L1_2$-Al_3M dispersoids. Under the T7A condition and prior creep test, base alloy B possessed the lowest number density of θ′ followed by alloy V2, while alloys Z2, ZV, and SZ exhibited much higher number densities of θ′ (Fig. 6 and Table 3). In addition, alloys Z2 and SZ contained a number of $L1_2$-Al_3M dispersoids, which could also effectively inhibit the dislocation movement. Therefore, when considering microstructure, it is expected that alloy B has the poorest creep resistance followed by alloy V2, and alloys Z2, ZV, and SZ show much improved creep resistance, which is generally in agreement with the results of creep tests (Fig. 8).

In addition to the microstructure before creep, the evolution of the microstructure during creep is also important for the creep resistance; the various microstructures of the crept samples are shown in Fig. 9.

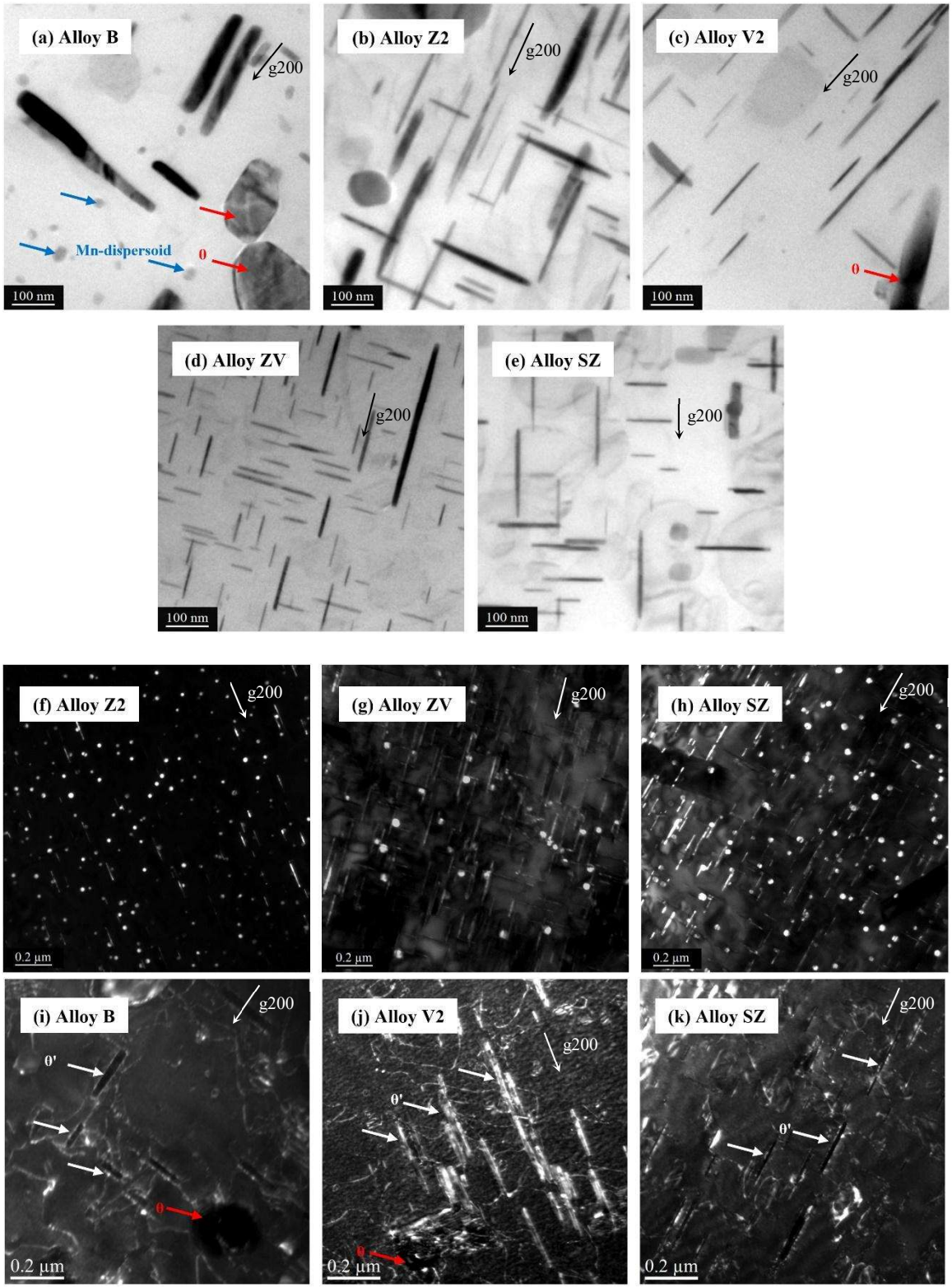
(a) Alloy B
g200
Mn-dispersoid
θ
100 nm
(b) Alloy Z2
g200
100 nm
(c) Alloy V2
g200
θ
100 nm
(d) Alloy ZV
g200
100 nm
(e) Alloy SZ
g200
100 nm
(f) Alloy Z2
g200
0.2 μm
(g) Alloy ZV
g200
0.2 μm
(h) Alloy SZ
g200
0.2 μm
(i) Alloy B
g200
θ'
θ
0.2 μm
(j) Alloy V2
g200
θ'
θ
0.2 μm
(k) Alloy SZ
g200
θ'
0.2 μm

Fig. 9. Distribution of θ′/ θ precipitates from bright-field TEM (a-e), $L1_2$-Al_3M dispersoids from dark-field TEM (f-h) and dislocations from weak-bean dark filed TEM (i-k) in the crept microstructure of experimental alloys

As shown in Fig. 9a, the θ′ in the crept sample of alloy B is severely coarsened and many large θ particles are observed (marked by red arrows), indicating that a large part of θ′ became unstable and was in the process to transform to the equilibrium incoherent θ phase during creep. This causes a much shorter primary and secondary creep stage (Fig. 8) compared to other alloys with TMs additions [46]. Owing to the continuous transformation from θ′ to the equilibrium θ phase in alloy B, the material displayed diminished resistance to restrain the dislocation movement, and its creep strain rate continued to increase during the "ternary stage" (Fig. 8c), resulting in the lowest creep resistance among all the alloys studied. Although some small Mn-containing dispersoids (indicated by black arrow) were observed in the matrix of alloy B after creep, they had little impact on the creep resistance because of their low volume fraction and scattered distribution.

In contrast, the degree of coarsening of θ′ in alloys with TMs is much lower than that of alloy B during creep deformation, which is most likely due to the segregation of TMs at the interface of θ′ to improve their thermal stability even under a load [9-11, 14, 16]. However, the different TMs and their combined additions have different impacts on the coarsening of θ′, and hence, on the creep resistance. In the alloy with individual V added (V2), in addition to the coarsened θ′, a small part of θ′ was transformed to the equilibrium θ phase after creep (marked by the red arrow in Fig. 9c), reducing the quantity of θ′, which explains its second-highest creep strain and minimum creep rate (Fig. 8). In the alloy with individual Zr added (Z2), θ′ was mainly in the coarsening process, and very rare equilibrium θ particles could be found (Fig. 9b). Although the size of θ′ in alloy Z2 was similar to that in alloy V2, the presence of a reasonable amount of Al_3Zr dispersoids (Fig. 9f) provided additional support to inhibit the dislocation motion during creep, resulting in a distinguishable reduction in both creep strain and minimum creep rate relative to alloy V2 (Fig. 8). In the alloys with combined additions of Zr and V (ZV) or Sc and Zr (SZ), θ′ was only slowly coarsening (Fig. 9d and 9e), showing the best thermal stability under the creep condition applied which is likely attributed to the combined contribution from the interfacial segregation of TM on θ' [10, 13, 14, 16, 17] and the formation of thermally

stable Al_3M dispersoids [14-16,19-21]. The number density of θ′ was considerably higher and the size of θ′ was finer in these two alloys than in other TM-added alloys (alloys V2 and Z2), leading to their superior creep resistance. In addition, a number of Al_3(Sc, Zr) dispersoids (Fig. 9h) in combination with finer θ′ in the SZ alloy greatly inhibited the dislocation movement, resulting in the best creep resistance among all the alloys studied. The weak-beam dark-field TEM images display the interaction between θ′ precipitates (or a combination of θ′ and Al_3(Sc, Zr)) and dislocations in the crept samples of alloys B, V2, and SZ (Fig. 9i – Fig. 9k). A large number of dislocations accumulated around the θ′ and θ particles in the crept alloys B and V2 (Fig. 9i and 9j). Due to the coarsening and transformation to incoherent θ, much less θ′ in the aluminum matrix was available to effectively restrain the dislocation motion and to cause the high mobility of dislocations, which was evidenced by high creep deformation with large creep strains after 100 h, e.g., 0.23 in alloy B and 0.04 in alloy V2, respectively. In contrast, a low number of dislocations was found around fine θ′ and Al_3(Sc, Zr) particles in the crept microstructure of alloy SZ, and the low mobility of dislocations resulted in ultralow creep deformation with a small creep strain (only 0.007 after 100 h).

It is worth mentioning that both Al_3Zr and Al_3(Sc, Zr) dispersoids in the Al–Cu alloy were thermally stable (Fig. 9f–h), and their number density and size remained almost unchanged under the current creep condition (50 MPa at 300 °C for 100 h). It has been confirmed in recent studies [14-16] that the significant contribution of $L1_2$-Al_3M dispersoids and the co-existence of two thermally stable precipitates (e.g., θ′ and $L1_2$-Al_3M) greatly improved the creep resistance of Al–Cu alloys. Other recent work [10] also indicated that the co-precipitation microstructure of $L1_2$-Al_3M and θ′ was highly stable in Al–Cu alloys and was a key factor governing microstructural stability beyond 300 °C.

5. Conclusions

1) The microalloying of Zr, V, and Sc in Al–Cu 224 cast alloys could generally delay the transformation from θ″ to θ′ during the T7 aging process and effectively increase the

coarsening resistance of θ' during prolonged thermal exposure at 300 °C for 100 h (T7A), especially in the alloys with combined TM additions.

2) The addition of Zr and Sc+Zr promoted the formation of $L1_2$-Al_3M dispersoids during solution treatment, which were thermally stable at 300 °C. No such dispersoids were observed in the alloy with individual V addition, and V further inhibited the homogeneous precipitation of $L1_2$-Al_3Zr when combined with Zr.
3) The W-AlScCu intermetallic phase was formed during solidification and solution treatment with Sc addition, which consumed the Cu and Sc solutes in the aluminum matrix and reduced the supersaturated level of Cu solutes during the T7 aging treatment, resulting in a deterioration of mechanical strength under T7 and T7A conditions.
4) The mechanical properties after T7A thermal exposure were greatly improved by the microalloying of Zr, V, and Sc because of the increased thermal stability of θ′ and the presence of $L1_2$-Al_3M dispersoids, which was rationalized by strengthening models.
5) In terms of elevated-temperature mechanical properties, the alloy with combined Zr+V addition achieved the highest yield strength at 300 °C after T7A, with an increase of 37% relative to the base alloy.
6) The microalloying of Zr, V, and Sc significantly increased the elevated-temperature creep properties. The alloy with microalloyed Sc+Zr obtained the best creep resistance with a minimum creep rate of 5.5×10^{-9} s^{-1} compared with 2.0×10^{-7} s^{-1} for the base alloy, owing to the co-existence of thermally stable θ′ precipitates and Al_3(Sc, Zr) dispersoids.

Acknowledgments

The authors would like to acknowledge the financial support of the Natural Sciences and Engineering Research Council of Canada (NSERC) under Grant No. CRDPJ 514651-17 and Rio Tinto Aluminum through the Research Chair in the Metallurgy of Aluminum Transformation at University of Quebec in Chicoutimi.

Data availability

The raw/processed data required to reproduce these findings cannot be shared at this time as the data also forms part of an ongoing study.

References

[1] P. Huter, P. Renhart, S. Oberfrank, M. Schwab, F. Grün, B. Stauder, High- and low-cycle fatigue influence of silicon, copper, strontium and iron on hypo-eutectic Al–Si–Cu and Al–Si–Mg cast alloys used in cylinder heads, International Journal of Fatigue 82 (2016) 588-601.
[2] S. Roy, L.F. Allard, A. Rodriguez, T.R. Watkins, A. Shyam, Comparative Evaluation of Cast Aluminum Alloys for Automotive Cylinder Heads: Part I—Microstructure Evolution, Metallurgical and Materials Transactions A 48(5) (2017) 2529-2542.
[3] S. Roy, L.F. Allard, A. Rodriguez, W.D. Porter, A. Shyam, Comparative Evaluation of Cast Aluminum Alloys for Automotive Cylinder Heads: Part II—Mechanical and Thermal Properties, Metallurgical and Materials Transactions A 48(5) (2017) 2543-2562.
[4] J.G. Kaufman, E.L. Rooy, Aluminum alloy castings: properties, processes, and applications, Asm International, 2004.
[5] L. Jin, K. Liu, X.G. Chen, Evolution of dispersoids and their effects on elevated-temperature strength and creep resistance in Al-Si-Cu 319 cast alloys with Mn and Mo additions, Materials Science and Engineering: A 770 (2020).
[6] A.R. Farkoosh, X. Grant Chen, M. Pekguleryuz, Dispersoid strengthening of a high temperature Al–Si–Cu–Mg alloy via Mo addition, Materials Science and Engineering: A 620 (2015) 181-189.
[7] J.G. Kaufman, Properties of aluminum alloys: tensile, creep, and fatigue data at high and low temperatures, ASM international, 1999.
[8] J. Rakhmonov, K. Liu, L. Pan, F. Breton, X.G. Chen, Enhanced mechanical properties of high-temperature-resistant Al–Cu cast alloy by microalloying with Mg, Journal of Alloys and Compounds 827 (2020) 154305.
[9] C. Yang, D. Shao, P. Zhang, Y.H. Gao, J.Y. Zhang, J. Kuang, K. Wu, G. Liu, J. Sun, The influence of Sc solute partitioning on ductile fracture of Sc-microalloyed Al-Cu alloys, Materials Science and Engineering: A 717 (2018) 113-123.
[10] J.D. Poplawsky, B.K. Milligan, L.F. Allard, D. Shin, P. Shower, M.F. Chisholm, A. Shyam, The synergistic role of Mn and Zr/Ti in producing θ′/L12 co-precipitates in Al-Cu alloys, Acta Materialia 194 (2020) 577-586.
[11] D. Shin, A. Shyam, S. Lee, Y. Yamamoto, J.A. Haynes, Solute segregation at the Al/θ′-Al2Cu interface in Al-Cu alloys, Acta Materialia 141 (2017) 327-340.
[12] J. Rakhmonov, K. Liu, G.X. Chen, Effects of Compositional Variation on the Thermal Stability of θ′-Al2Cu Precipitates and Elevated-Temperature Strengths in Al-Cu 206 Alloys, Journal of Materials Engineering and Performance 29(11) (2020) 7221-7230.
[13] A. Shyam, S. Roy, D. Shin, J.D. Poplawsky, L.F. Allard, Y. Yamamoto, J.R. Morris, B. Mazumder, J.C. Idrobo, A. Rodriguez, T.R. Watkins, J.A. Haynes, Elevated temperature

microstructural stability in cast AlCuMnZr alloys through solute segregation, Materials Science and Engineering: A 765 (2019).
[14] Y.H. Gao, C. Yang, J.Y. Zhang, L.F. Cao, G. Liu, J. Sun, E. Ma, Stabilizing nanoprecipitates in Al-Cu alloys for creep resistance at 300°C, Materials Research Letters 7(1) (2018) 18-25.
[15] Y.H. Gao, L.F. Cao, C. Yang, J.Y. Zhang, G. Liu, J. Sun, Co-stabilization of θ'-Al_2Cu and Al_3Sc precipitates in Sc-microalloyed Al–Cu alloy with enhanced creep resistance, Materials Today Nano 6 (2019).
[16] C. Yang, L. Cao, Y. Gao, P. Cheng, P. Zhang, J. Kuang, J. Zhang, G. Liu, J. Sun, Nanostructural Sc-based hierarchy to improve the creep resistance of Al–Cu alloys, Materials & Design 186 (2020).
[17] C. Yang, P. Zhang, D. Shao, R.H. Wang, L.F. Cao, J.Y. Zhang, G. Liu, B.A. Chen, J. Sun, The influence of Sc solute partitioning on the microalloying effect and mechanical properties of Al-Cu alloys with minor Sc addition, Acta Materialia 119 (2016) 68-79.
[18] P. Shower, J. Morris, D. Shin, B. Radhakrishnan, J. Poplawsky, A. Shyam, Mechanisms for stabilizing θ′(Al_2Cu) precipitates at elevated temperatures investigated with phase field modeling, Materialia 6 (2019).
[19] S. Kumar Makineni, S. Sugathan, S. Meher, R. Banerjee, S. Bhattacharya, S. Kumar, K. Chattopadhyay, Enhancing elevated temperature strength of copper containing aluminium alloys by forming L12 Al3Zr precipitates and nucleating theta" precipitates on them, Sci Rep 7(1) (2017) 11154.
[20] S. Mondol, S.K. Makineni, S. Kumar, K. Chattopadhyay, Enhancement of High Temperature Strength of 2219 Alloys Through Small Additions of Nb and Zr and a Novel Heat Treatment, Metallurgical and Materials Transactions A 49(7) (2018) 3047-3057.
[21] B. Rouxel, M. Ramajayam, T.J. Langan, J. Lamb, P.G. Sanders, T. Dorin, Effect of dislocations, Al3(Sc,Zr) distribution and ageing temperature on θ′ precipitation in Al-Cu-(Sc)-(Zr) alloys, Materialia 9 (2020).
[22] C. Li, K. Liu, X.G. Chen, Improvement of elevated-temperature strength and recrystallization resistance via Mn-containing dispersoid strengthening in Al-Mg-Si 6082 alloys, Journal of Materials Science & Technology 39 (2020) 135-143.
[23] K. Liu, X.G. Chen, Development of Al–Mn–Mg 3004 alloy for applications at elevated temperature via dispersoid strengthening, Materials & Design 84 (2015) 340-350.
[24] K. Liu, H. Ma, X.G. Chen, Enhanced elevated-temperature properties via Mo addition in Al-Mn-Mg 3004 alloy, Journal of Alloys and Compounds 694 (2017) 354-365.
[25] Z. Li, Z. Zhang, X.G. Chen, Improvement in the mechanical properties and creep resistance of Al-Mn-Mg 3004 alloy with Sc and Zr addition, Materials Science and Engineering: A 729 (2018) 196-207.
[26] P.M. Kelly, K. Pm, Quantitative electron microscopy, METALS FORUM 5 (1982) 13-23.
[27] J.F. Nie, B.C. Muddle, Strengthening of an Al–Cu–Sn alloy by deformation-resistant precipitate plates, Acta Materialia 56(14) (2008) 3490-3501.
[28] J.W. Cahn, J. NuttIng, Transmission quantitative metallography, Transactions of The American Institute of Mining and Metallurgical Engineers 215(3) (1959) 526-528.
[29] K. Liu, X. Cao, X.G. Chen, Effect of Mn, Si, and cooling rate on the formation of iron-rich intermetallics in 206 Al-Cu cast alloys, Metallurgical and Materials Transactions B 43(5) (2012) 1231-1240.

[30] C. Shi, X.G. Chen, Effect of vanadium on hot deformation and microstructural evolution of 7150 aluminum alloy, Materials Science and Engineering: A 613 (2014) 91-102.
[31] K. Liu, X. Cao, X.G. Chen, Solidification of Iron-Rich Intermetallic Phases in Al-4.5Cu-0.3Fe Cast Alloy, Metallurgical and Materials Transactions A 42(7) (2011) 2004-2016.
[32] X. Liu, Z. Guo, J. Xue, C. Zhu, Effects of cooling rate on casting ternary Al–Cu-Sc alloy prepared by ultrasound-assisted molten salt electrolysis, Materials Science and Engineering: A 771 (2020).
[33] I. Zuiko, R. Kaibyshev, Aging behavior of an Al–Cu–Mg alloy, Journal of Alloys and Compounds 759 (2018) 108-119.
[34] J. Rakhmonov, G. Timelli, F. Bonollo, The Effect of Transition Elements on High-Temperature Mechanical Properties of Al–Si Foundry Alloys–A Review, Advanced Engineering Materials 18(7) (2016) 1096-1105.
[35] K.E. Knipling, D.C. Dunand, D.N. Seidman, Criteria for developing castable, creep-resistant aluminum-based alloys–A review, Zeitschrift für METALLKUNDE 97(3) (2006) 246-265.
[36] Y. Fan, M.M. Makhlouf, Precipitation strengthening in aluminum-zirconium-vanadium alloys, Journal of Alloys and Compounds 725 (2017) 171-180.
[37] J.D. Boyd, R. Nicholson, The coarsening behaviour of θ ″and θ′ precipitates in two Al-Cu alloys, Acta Metallurgica 19(12) (1971) 1379-1391.
[38] L. Pan, K. Liu, F. Breton, X.G. Chen, Effect of Fe on microstructure and properties of 8xxx aluminum conductor alloys, Journal of Materials Engineering and Performance 25(12) (2016) 5201-5208.
[39] F.R.N. Nabarro, Creep in commercially pure metals, Acta Materialia 54(2) (2006) 263-295.
[40] T. Gladman, Precipitation hardening in metals, Materials Science and Technology 15(1) (2013) 30-36.
[41] J.G. Kaufman, Introduction to aluminum alloys and tempers, ASM international, 2000.
[42] O. Engler, C.D. Marioara, Y. Aruga, M. Kozuka, O.R. Myhr, Effect of natural ageing or pre-ageing on the evolution of precipitate structure and strength during age hardening of Al–Mg–Si alloy AA 6016, Materials Science and Engineering: A 759 (2019) 520-529.
[43] J. Qin, Z. Zhang, X.G. Chen, Mechanical Properties and Strengthening Mechanisms of Al-15 Pct B4C Composites with Sc and Zr at Elevated Temperatures, Metallurgical and Materials Transactions A 47(9) (2016) 4694-4708.
[44] A.W. Zhu, A. Csontos, E.A. Starke Jr, Computer experiment on superposition of strengthening effects of different particles, Acta materialia 47(6) (1999) 1713-1721.
[45] G.E. Dieter, D.J. Bacon, Mechanical metallurgy, McGraw-hill New York, 1986.
[46] Y. Xu, L. Yang, L. Zhan, H. Yu, M. Huang, Creep Mechanisms of an Al-Cu-Mg Alloy at the Macro- and Micro-Scale: Effect of the S'/S Precipitate, Materials (Basel) 12(18) (2019).